Factors Determining the Frequency of El Niño

Zhuoxin Gu[a] and De-Zheng Sun[b]

[a] *Department of Atmospheric and Oceanic Sciences/Institutes of Atmospheric Sciences, Fudan University, Shanghai, 200438, China*

[b] *Nanjing-Helsinki Institute in Atmospheric and Earth System Sciences, Nanjing University-Suzhou Campus, Suzhou, 215163, China*

J. Climate

(Submitted:15 January; Revised: 9 May; Revised 15 July; Accepted: 30 July 2025)

Corresponding author: De-Zheng Sun, dezheng.sun@nju.edu.cn

ABSTRACT

Observations and model simulations indicate long-term changes in the frequency of El Niño events, but explanations for these changes diverge. This divergence underscores that the frequency of El Niño has not been understood as well as some earlier ENSO theories suggested. Here, we investigate factors controlling the frequency of El Niño by employing a nonlinear box model capable of simulating a broad range of observed ENSO properties, including the asymmetry between its two phases. The model includes multiple parameters, each corresponding to a distinct and well-defined physical processes. One of these parameters is the radiative-convective equilibrium SST, which measures the intensity of radiative heating exerted upon the coupled tropical ocean-atmosphere system. Other parameters are the dynamical coupling strength between the atmosphere and ocean, the thermal damping coefficient from the atmosphere, the strength of zonal advection relative to upwelling, and the dynamical adjustment time-scale for the upper ocean. Sensitivity experiments show that El Niño frequency depends as much as on the intensity of radiative heating as on other parameters. A fundamental mechanism by which the intensity of radiative heating affects the frequency of El Niño is its effect on the generation of increasingly complex limit cycles, which in turn alters oscillation patterns. These findings highlight fundamental limitations of linear approaches to address the problem of El Niño frequency. They also provide insight into how a change in the intensity of radiative heating, such as that induced by a change in the greenhouse effect, may alter the frequency of El Niño.

SIGNIFICANCE STATEMENT

Factors determining the frequency of El Niño are not yet fully understood. Existing theories and the state-of-the-art models do not agree on the key factors that influence El Niño frequency. Sensitivity experiments with a nonlinear box model reveal that El Niño frequency depends on several factors that correspond to well-defined physical processes, including the intensity of radiative heating. A fundamental mechanism by which the intensity of radiative heating affects El Niño frequency is its impact on the generation of increasingly complex limit cycles, which in turn alters oscillation patterns. The results highlight the critical role of nonlinearity in determining the frequency of El Niño. They also shed light on how the intensity of radiative heating may influence El Niño frequency.

1. Introduction

It is crucial to have a thorough understanding of what controls the frequency of El Niño events. El Niño affects global climate, including extreme weather events (Arblaster and Alexander 2012; Thirumalai et al. 2017; Wang et al. 2017a; Rodríguez-Morata et al. 2019; Gao et al. 2020). Observations indicate that the frequency of El Niño changes on decadal and longer time-scales (An and Wang 2000; Fedorov and Philander 2000; McPhaden 2012; Hu et al. 2013; Capotondi and Sardeshmukh 2017; Hu et al. 2017a; Hu et al. 2017b). Projections from state-of-the-art fully coupled climate models suggest that extreme El Niño events may occur more frequently as global warming progresses (Cai et al. 2014; Cai et al. 2017; Wang et al. 2017b; Wang et al. 2019; Cai et al. 2021; Shin et al. 2022; Pathirana et al. 2023). These findings from the observations and models highlight the need to understand what are the factors involved in determining how often El Niño occurs.

However, factors that may be involved in determining the frequency of El Niño have not been fully understood. Existing theories differ on the key factors that are important in determining the frequency of occurrence of El Niño events. The delayed oscillator (Battisti 1988; Suarez and Schopf 1988) underscores the importance of the transit time of Rossby waves across the Pacific basin, and thereby the width of the basin. The recharge oscillator (Jin 1996), on the other hand, emphasizes the time required for the western tropical Pacific to refill its heat content or the dynamical adjustment time-scale for the equatorial upper ocean. The western Pacific oscillator (Weisberg and Wang 1997) is similar to the delayed oscillator in spirit, but adds a role for the Kelvin waves forced by the easterly anomalies over the western Pacific in terminating an El Niño event. The western Pacific oscillator also highlights the importance of local air-sea interactions over the off-equatorial western Pacific, which is lacking in the delayed oscillator theory. The advective-reflective oscillator (Picaut et al. 1997) is also similar to the delayed oscillator, but conceptualizes El Niño as a movement/expansion of the western Pacific warm-pool, thereby revealing the potentially important role of zonal advection. The stochastic theory (Penland and Sardeshmukh 1995; Penland 1996; Kleeman 2008; Thual et al. 2016) argues that ENSO variability can be simulated by a stable linear system forced by weather noise, and highlights the critical role of stochastic forcing. Sun (1997) and his collaborators (Liang et al. 2012; Hua et al. 2019) attributed the existence of El Niño to the fact that there are two equilibria for the coupled tropical Pacific, but under the present intensity of radiative heating, both of the equilibria become unstable, resulting in an apparent “wandering” behavior

for the tropical Pacific. This inherently nonlinear perspective strongly suggests that multiple processes influence the frequency of El Niño, including external forcing, such as the intensity of radiative heating, or the efficiency of dissipative processes, such as the thermal damping coefficient. Changes in these factors can alter the dynamic regimes of the system. However, a systematic investigation of how the frequency of El Niño in this model is determined has not yet been conducted. The aforementioned theories, when viewed individually, all have persuasive elements. However, it is also evident that they do not have the same prognosis for the factors controlling the El Niño frequency.

The question concerning the frequency of El Niño has also been studied using fully coupled GCMs, but these more sophisticated models do not appear to agree on the key factors influencing ENSO frequency either (Yeh et al. 2009; Cai et al. 2014; Cai et al. 2017; Wang et al. 2017b; Wang et al. 2019; Shin et al. 2022; Pathirana et al. 2023). By using CMIP3 models, Yeh et al. (2009) inferred that a flattening of the thermocline in the equatorial Pacific under global warming could increase the frequency of El Niño. Using CMIP5 outputs, Cai et al. (2014, 2017) revealed that an increased frequency of extreme El Niño events under global warming and they attributed this change to a faster warming in the eastern Pacific compared to the surrounding oceans, including the central Pacific. Wang et al. (2017b) suggested that oceanic thermocline deepening may be an underlying cause for the continued increase in the frequency of extreme El Niño events after the 1.5°C warming stabilization. Wang et al. (2019), on the other hand, suggested that warming in the western Pacific might lead to more frequent occurrence of extreme El Niño events. Shin et al. (2022) and Pathirana et al. (2023) suggested that the intensified nonlinear response of rainfall to sea surface temperature changes may be a key factor for the increased frequency of extreme El Niño events under global warming. Even such a short review makes it evident that the results from the fully coupled models are also more scattered than desired. Additionally, studies using fully coupled GCMs often implicitly assume that changes in the mean state can predict changes in ENSO frequency (An and Wang 2000; Fedorov and Philander 2000; Deng et al. 2010). However, some studies suggest that changes in the mean state may be caused by changes in the frequency/magnitude of El Niño (Sun and Zhang 2006; Sun 2007; Liang et al. 2012; Sun et al. 2014). For instance, in a numerical experiment with a coupled model, Sun (2007) and his collaborators (Sun and Zhang 2006; Sun et al. 2014) found that the decadal warming over the upper ocean is due to the rectification effect of elevated ENSO events on the mean state. Similar results were obtained by Liang et al. (2012) using a box model based on Sun (1997). Moreover, there are some

common biases in the simulation of ENSO by the state-of-the-art climate models. For example, the asymmetry of ENSO is found to be commonly underestimated in these models (Sun et al. 2013; Zhang and Sun 2014; Sun et al. 2016; Hayashi et al. 2020; Zhao and Sun 2022). These studies further the impression that our understanding of factors controlling the frequency of El Niño is likely still in an adolescent stage—ready for rapid development, but not yet mature.

The simple box model of Sun (1997), though originally developed to suggest a potentially fundamental role of the intensity of radiative heating in the very existence of El Niño, has been shown by later studies to be able to capture many observed characteristics of ENSO, including the asymmetry of ENSO and its decadal variations (Timmermann and Jin 2002; Kim and An 2011; Liang et al. 2012; Roberts et al. 2016; Guckenheimer et al. 2017; Kohyama and Hartmann 2017; Liang et al. 2017; Ray et al. 2020). Though not always emphasized in later studies, the key to the Sun model's ability to capture complex behavior of the ENSO system, such as the asymmetry between its two phases, is the existence of two equilibria. It is the first model of this kind to include the coupling between the surface western Pacific and the surface eastern Pacific as a fundamental component of ENSO dynamics, as essential as the thermocline adjustment to wind forcing emphasized in the recharge oscillator model (Jin 1996). The resulting three predictive equations in the model of Sun (1997) have also led to a fundamentally nonlinear explanation of why ENSO takes place—the birth of a limit cycle when the external conditions meet the internal requirements or the internal properties align with the external conditions. We will see that changes in external forcing, such as the intensity of radiative heating, or in the internal properties of the system—like the coupling strength or the thermal damping efficiency—do not just result in a single loop of limit cycles. Instead, multiple loop limit cycles are generated, creating more complex oscillation patterns, some of which closely resemble those observed in the time series of eastern equatorial Pacific SST.

Moreover, the major physical parameters in the model of Sun (1997) correspond to well-defined physical processes, including one for the intensity of radiative heating—the radiative-convective equilibrium SST. However, later studies with the use of this model have mostly focused on the zonal advection inclusion in the model—or more accurately, the inclusion of the coupling between the two surface oceans in the tropical Pacific. The model of Sun (1997) is not an anomaly model. In particular, it allows the subsurface to "feel" a change in the radiative-convective equilibrium temperature (or a change in the deep ocean temperature). The upper ocean in the model is effectively heated from above by the Sun and the greenhouse effect,

and cooled from below by the deep ocean. The model's configuration enables an investigation of the role of the intensity of radiative heating, albeit in a still primitive way. In this regard—emphasizing the heat transfer aspect of the ENSO system, the model, though also nonlinear, differs fundamentally from some earlier nonlinear models (Chang et al. 1994; Jin et al. 1994; Tziperman et al. 1994; Wang and Fang 1996; Tziperman et al. 1997). We aim to understand the role of all major parameters in determining the frequency of El Niño in the model of Sun (1997), particularly the role of the intensity of radiative heating.

Compared to fully coupled GCMs—the most sophisticated tools currently used to study El Niño (Deser et al. 2012; Eyring et al. 2016; Capotondi et al. 2020; Fredriksen et al. 2020, and others)—the model of Sun (1997) is highly simplified. However, it can simulate some complex aspects of ENSO that even the most advanced models, such as the CMIP6 models, still struggle with (Timmermann and Jin 2002; Liang et al. 2012, 2017; Hayashi et al. 2020; Zhao and Sun 2022, and others).

To be clear, CMIP6 models provide much more detailed information, and simple models like that of Sun (1997) are not intended to replace more sophisticated climate models. As Held (2005) emphasized, understanding complex climate phenomena requires the use of a hierarchy of models. The use of a simple model—one capable of capturing complex behavior—to study the problem of El Niño aligns with the approach advocated by Held (2005) and others. We anticipate that a study using this box model can complement those based on more sophisticated models, such as those employed by prominent researchers in this field (Deser et al. 2012; Eyring et al. 2016; Capotondi et al. 2020; Fredriksen et al. 2020, and others). Like other box models, the Sun model enables sensitivity experiments to be conducted with precision and over a range that are not easily achievable with fully coupled GCMs.

In this study, we will use the model of Sun (1997) as a starting point to further advance our understanding of factors influencing the frequency of El Niño. The paper is organized as follows. In Section 2, we briefly describe the methodology, including some technical details of the Sun model as they pertain to the present study. In Section 3, we present the sensitivity experiments to understand the dependence of the frequency of El Niño on changes in various parameters representing different physical processes. A summary and discussion are provided in Section 4.

2. Methodology

Our main methodology here is to conduct sensitivity experiments with the box model of Sun (1997). The model may be regarded as the lowest-order representation of the coupled tropical ocean-atmosphere system. It consists of five boxes: two for the surface ocean—representing the western and eastern equatorial Pacific, respectively; two for the subsurface upper ocean; and one for the deep ocean. The basic setup of the box model of Sun (1997) is that it is heated from above by the solar radiation and the greenhouse effect in the atmosphere, and cooled from below, as the equatorial upper ocean sits on a deep ocean with a fixed temperature. The intensity of radiative heating is measured by the radiative-convective equilibrium temperature T_e—the SST that the ocean would attain if there were no ocean dynamics. The ocean-atmosphere in the model is dynamically coupled through the Bjerknes chain reaction—upwelling is proportional to the equatorial zonal winds, which are in turn proportional to the zonal SST contrast. The dynamical coupling strength is measured by a parameter called α. The surface heat flux is parameterized by a restoring boundary condition, and the restoring time-scale is measured by $1/c$, which is also the time-scale for the atmosphere process to damp an SST anomaly. Zonal advection is related to total upwelling through a parameter called s, which is the ratio between the zonal flux and total upwelling. Another important parameter is $1/r$, which measures the dynamical adjustment time-scale for the equatorial upper ocean. The full set of equations for the Sun model is provided in the Appendix.

Focusing on the goal of illustrating the potential importance of the intensity of radiative heating in giving rise to the existence of El Niño, Sun (1997) only examined the response of the model to variations in T_e. Sun (1997) showed that for very low values of T_e, the model has one equilibrium state, which is zonally symmetric. As T_e increases to a critical value, a pitch-fork bifurcation takes place, generating a second equilibrium, which is zonally asymmetric. With further increases in T_e, the zonal SST contrast becomes increasingly large. When the zonal SST contrast becomes sufficiently large, a Hopf bifurcation occurs that generates a limit cycle which enables the system to oscillate. From the perspective of the nonlinear model, the existence of El Niño is due to the fact that both equilibrium states are unstable under the current intensity of radiative heating. The instability of the zonally asymmetric equilibrium results in a limit cycle.

In analyzing the time series, Sun (1997) focused his attention on the immediate neighborhood of the Hopf bifurcation. He also focused on the issue of the dependence of magnitude of El Niño rather than on the issue of the frequency of its occurrence. In this paper, we will examine the latter issue by carefully investigating whether there are additional dynamic regimes within the oscillatory regime he identified.

In addition to T_e, we will also examine the role of the other four aforementioned parameters —α, $1/c$, s, and $1/r$—in determining the frequency of El Niño. Our working hypothesis, in light of non-dimensional analysis of Sun (1997) (see also Liang et al. 2012), is that all these parameters may play an important role. We also anticipate that the nonlinearity in the system may make the dependence on these parameters nonlinear. When varying each of the five parameters, the other four are kept fixed. The remaining parameters are the same as those in Sun (1997).

As pointed out by Trenberth back in 1997, there is no universal way to identify an El Niño event from observations. Many observational studies, for convenience, have equated the occurrence of a lasting positive SST anomaly relative to the long-term climatology with an occurrence of El Niño. The plus side of this approach is that it conforms the conceptual view that El Niño corresponds to anomalous warming in the tropical eastern Pacific. The potential downside is that it may obscure the dynamics behind El Niño, given accumulating evidence suggesting that the climatology is a function of El Niño events (Sun and Zhang 2006; Sun 2007; Liang et al. 2012; Sun et al. 2014). These studies, in particular that of Liang et al. (2012), highlight that the climatological state of a system is not the same as an equilibrium state of the system. If El Niño indeed results fundamentally from a bifurcation of the system—the generation of a limit cycle from the instability of an equilibrium state (or the instability of a limit cycle so generated)—then an El Niño event may be defined as a lasting and significant excursion from this equilibrium point. This definition of El Niño is schematically shown in Fig. 1. The difficulty in applying this view to observations is that we do not know exactly where the equilibrium state is. The nonlinear model we use, however, allows us to accurately calculate the equilibrium state—even when it is an unstable one. So, we will take advantage of this fact. As indicated in Fig. 1, when the eastern equatorial Pacific SST (T_2) is greater than its equilibrium value, it signals the occurrence of an El Niño event. When T_2 falls below its equilibrium value, it signals the end of an El Niño event.

Here, we use the concept of return period (marked by RP), defined as the average time interval between two adjacent El Niño events—to measure the average frequency of El Niño events. It is calculated by first identifying and counting the total number of El Niño events (N) within a sufficiently long period (P). RP is then obtained by dividing P by N. This applies to a situation where there is a single loop limit cycle as well as to a situation with a limit cycle consisting of multiple loops. As we will see, the time series of eastern equatorial Pacific SST (T_2) in the latter situation is characterized by strong El Niño events interspersed with weaker El Niño events. In this paper, we are only interested in the average return period of all El Niño events. Return periods stratified by the magnitude of El Niño events will be reported in future studies. By a sufficiently long period, we mean that P is large enough for a stable RP—further increases in P do not change the value of RP.

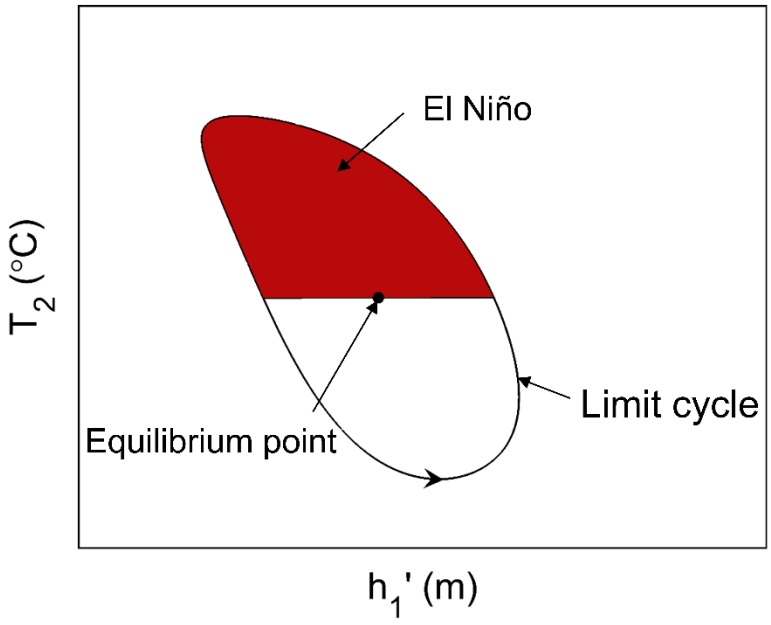

Fig. 1. A schematic illustration for the definition of El Niño used in this study. The circle represents a single-loop of a limit cycle (a limit cycle can have two or more loops). T_2 is the SST for the eastern equatorial Pacific, and $h_1^{'}$ is the thermocline depth in the western equatorial Pacific relative to a reference value for the zonal mean depth of the upper ocean (Sun 1997). The black dot indicates the equilibrium state whose instability generates a limit cycle. The red area, where T_2 is greater than its equilibrium value corresponding to this equilibrium state, indicates an El Niño event.

3. Results

a. The dependence of El Niño frequency on the intensity of radiative heating

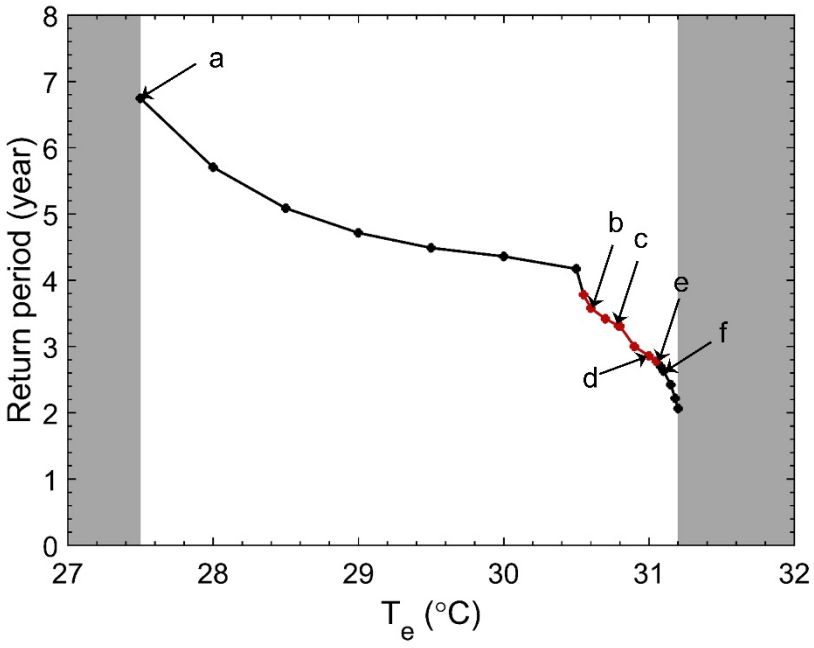

Fig. 2. The dependence of the frequency of El Niño on the value of the radiative-convective equilibrium temperature (T_e). The frequency of El Niño is measured here by the return period of El Niño. Note that the shorter the return period, the higher the frequency. The dots in the figure marked by a, b, c, d, e, and f are respectively where the time series shown in Fig. 3a, Fig. 3b, Fig. 3c, Fig. 3d, Fig. 3e, and Fig. 3f are taken. The black dots indicate the regimes with a single-loop limit cycle (and therefore a strictly periodic oscillation), while the red dots indicate the regimes with two-loop or multi-loop limit cycles. The shaded area indicates steady regimes with no oscillations. While varying the value of T_e, α/a, s, $1/r$, and $1/c$ are fixed respectively to 3.0×10^{-8} K^{-1} s^{-1}, 0.096, 300 days, and 150 days. Other parameters in the model are the same as in Sun (1997).

As the intensity of radiative heating—measured by the radiative-convective equilibrium SST (T_e)—increases, El Niño events occur more frequently, characterized by shorter return periods. Fig. 2 illustrates the frequency of occurrence of El Niño events, measured by the return period of SST in the eastern equatorial Pacific (T_2). The range of T_e within which the system can generate oscillations spans from 27.5 to 31.2°C. Within this oscillatory regime, the variation in frequency with respect to changes in the value of T_e is highly nonlinear. This nonlinear phenomenon seems to be related to the existence of multiple dynamic regimes in the model, and the dependence of the frequency on T_e varies in different regimes. For small values of T_e (T_e smaller than 30.6°C), the system is in a regime with a gradual increase in frequency (decrease in return period RP). When T_e increases to around 30.6°C, a steep change in frequency occurs owing to a period doubling bifurcation, marking the transition to another

regime where the frequency increases more rapidly than in the previous regime. This regime is represented by the red dots in the figure, indicating the presence of a limit cycle with two or more loops in the system. As T_e continues to rise to about 31.10℃, another abrupt change in frequency takes place as the system returns to a regime with a single-loop limit cycle, and the system enters a regime characterized by the most rapid increase in frequency.

T_e may be regarded as the tropical maximum SST, which occurs in the western tropical Pacific (Sun 1997, 2003; Kim and An 2011). Since 1950, the highest monthly tropical Pacific SST recorded in observations from three leading SST datasets—HadISST v1.1 (Rayner et al. 2003), ERSST v5 (Huang et al. 2017), and COBE-SST 2 (Hirahara et al. 2014) are respectively 31.20°C, 30.85℃ and 31.05℃.

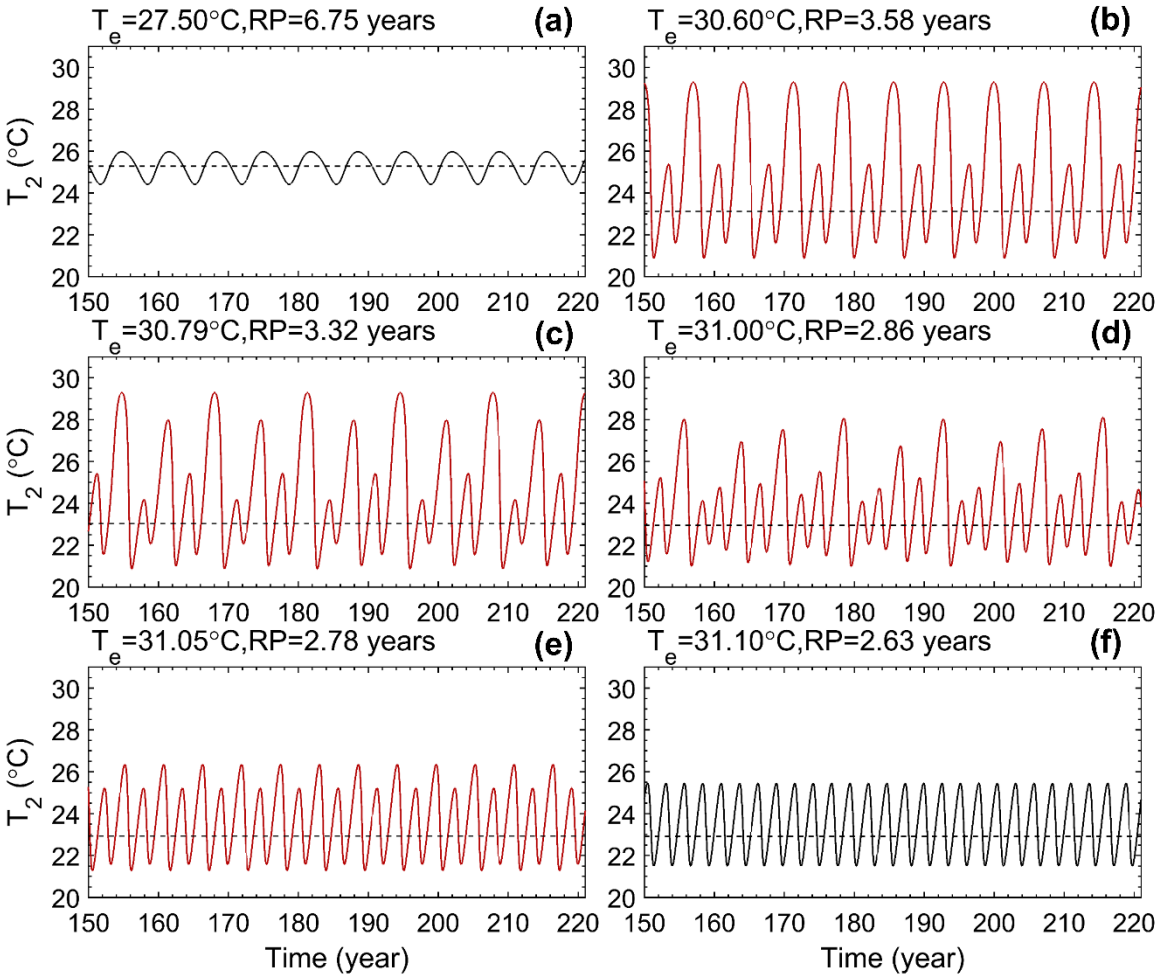

Fig. 3. Time series of the eastern equatorial Pacific SST (T_2) under different values of the radiative-convective equilibrium temperature (T_e). The corresponding values of the return period (RP) for El Niño events are indicated at the top of the time series. The time series shown in Fig. 3a, Fig. 3b, Fig. 3c, Fig. 3d, Fig. 3e, and Fig. 3f correspond to the dots marked a, b, c,

d, e, and f in Fig. 2. Time series with two or more different El Niño magnitudes are shown in red. The dashed line corresponds to the equilibrium value of T_2.

Figure 3 further illustrates that as T_e increases, the system undergoes multiple dynamic regimes, characterized by different oscillation patterns. The frequency depends on the dynamic regime the system is in, which in turn is determined by the value of T_e. For T_e=27.50°C, the oscillations of T_2 (Fig. 3a) exhibit a single magnitude, with an interval of approximately 6.75 years between two El Niño events. When T_e increases to 30.60°C, the oscillations (Fig. 3b) show an additional weaker event occurring between two stronger ones, resulting in a pattern that repeats every two cycles. The return period in this case is about 3.58 years, while the interval between strong El Niño events remains approximately 7.16 years. At T_e=30.79°C, the oscillation becomes more complex (Fig. 3c), featuring four different magnitudes of El Niño events. The return period shortens to 3.32 years, compared to 3.58 years in Fig. 3b. When T_e increases further to 31.00°C (Fig. 3d), the system exhibits the most complex oscillation pattern, with multiple weaker events of varying magnitudes occurring between the strongest warm events. The return period decreases to 2.86 years. If T_e increases to 31.05°C (Fig. 3e), the oscillation returns to the same pattern as that in Fig. 3b, but with shorter return period (RP=2.78 years). Finally, when the value of T_e is 31.10°C (Fig. 3f), the oscillation in the system returns to the same pattern as that in Fig. 3a, featuring warm events of uniform magnitude.

A fundamental mechanism by which T_e influences the frequency of El Niño is through its impact on the generation of a series of increasingly complex limit cycles, thereby altering oscillation patterns. At T_e=27.50°C, the trajectory in phase space is represented by a single-loop limit cycle (Fig. 4a), corresponding to periodic oscillations in the time series (Fig. 3a). The corresponding power spectrum is featured by a single dominant frequency approximately at f_0~1/6.75 year^{-1} (Fig. 5a). When T_e is set to 30.60°C, the trajectory in the phase space is characterized by a two-loop structure (Fig. 4b), reflected in the time series as oscillations of two distinct amplitudes (Fig. 3b). The dominant frequency (f_0) is about 1/3.58 year^{-1} and there is another spectral peak at a lower frequency ($f_0/2$) of about 1/7.16 year^{-1}. Further increases in T_e from 30.60°C result in the emergence of a four-loop limit cycle (Fig. 4c), manifested as oscillations with four distinct amplitudes in the time series (Fig. 3c), apparently through a period-doubling bifurcation. After a cascade of bifurcations, the system eventually transitions

to a multi-loop limit cycle, forming what is known as a strange attractor (Lorenz 1963; Strogatz 2015) (Fig. 4d). And these loops present themselves as multiple peaks in the power spectrum (Fig. 5d). With further increases in T_e, the instability of the limit cycle changes, and the system gradually transitions back to a two-loop limit cycle (Fig. 4e), ultimately returning to a single-loop limit cycle (Fig. 4f). This can be considered as a reversed period-doubling process, which manifests in the power spectrum as the transition from two peaks (Fig. 5e) to a single peak (Fig. 5f).

The regimes where the limit cycle experiences instability correspond to regimes with rapid increases in the frequency of occurrence of El Niño, as depicted by the red dots in Fig. 2. Note that the model we use is a three-dimensional one, with the corresponding three dimensions being T_1, T_2, and $h_1^{'}$. The trajectory shown in Fig. 4 is only a 2D projection.

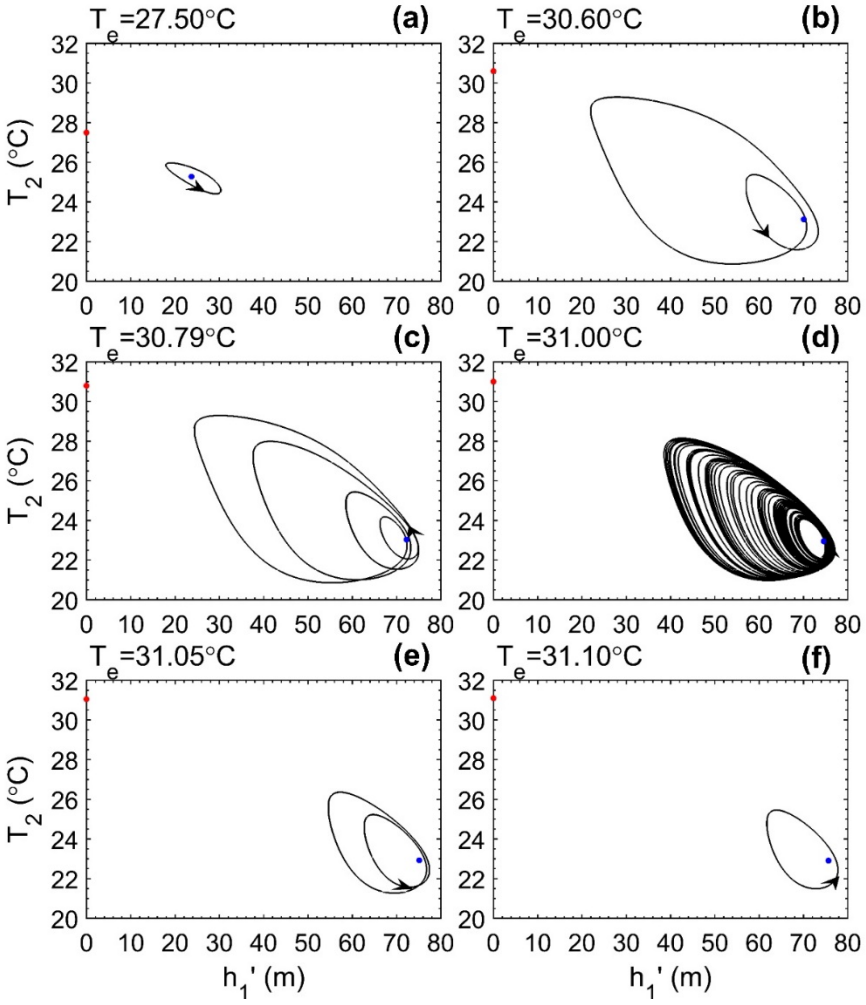

Fig. 4. The phase space trajectory of the system under different values of radiative-convective equilibrium SST (T_e). Shown are projections onto the plane of the thermocline

depth of western Pacific (h_1') and SST of the eastern equatorial Pacific (T_2). The trajectories shown in Fig. 4a, Fig. 4b, Fig. 4c, Fig. 4d, Fig. 4e, and Fig. 4f correspond to the dots marked a, b, c, d, e, and f in Fig. 2. The red and blue dots represent the two equilibrium states of the system.

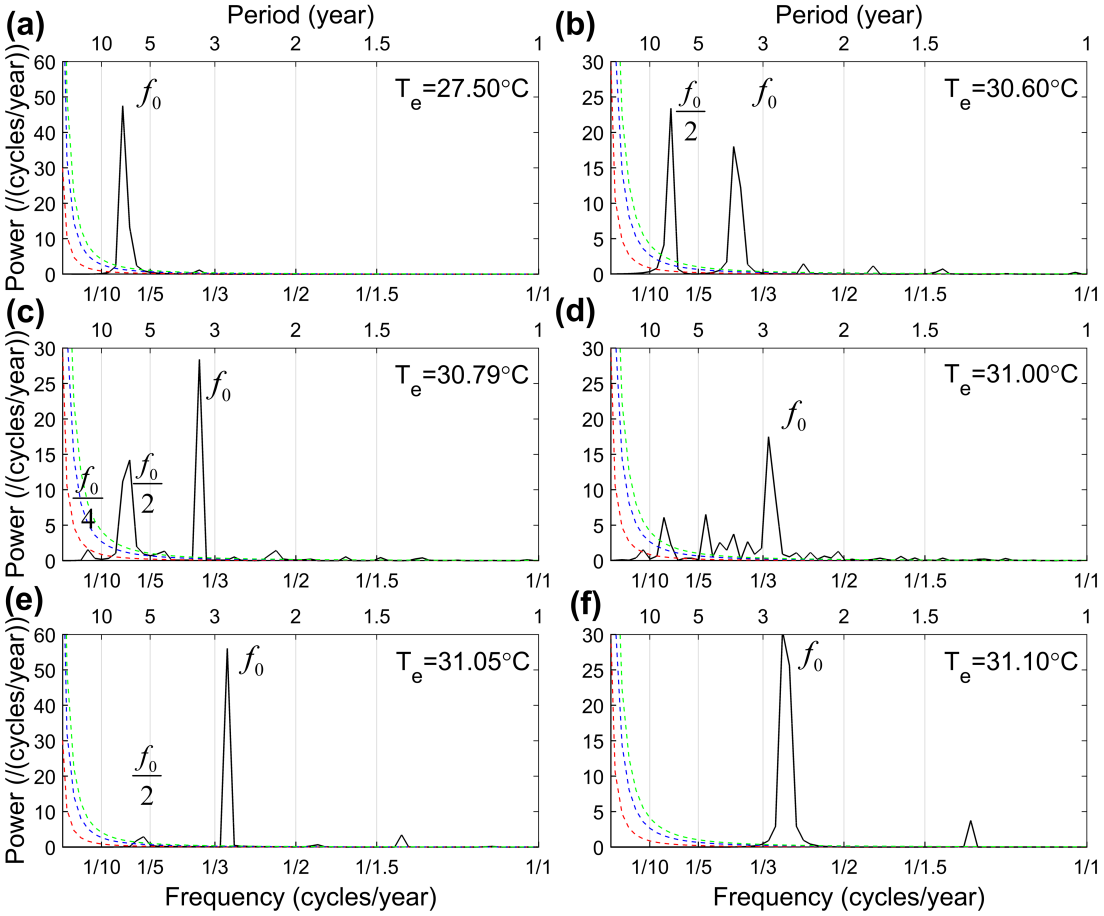

Fig. 5. The power spectrum of the time series of the eastern equatorial Pacific SST (T_2) in simulations with different values of radiative-convective equilibrium SST (T_e). f_0 marks the dominant frequency. Also shown are the best-fit AR (1) spectrum (red) along with its 99% and 95% confidence bounds (green and blue dashed lines, respectively). The top axis indicates the period in years, while the bottom axis represents the frequency in cycles per year. For each simulation, the corresponding T_e to which the model is subjected is noted in the top-right corner. A 75-year dataset is used for this spectrum calculation.

b. The dependence of El Niño frequency on the dynamical coupling strength

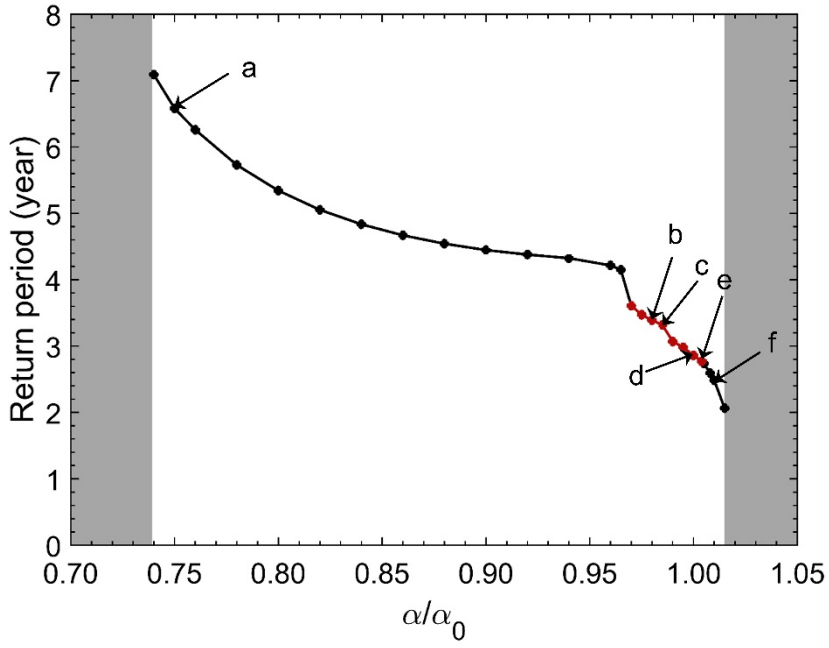

Fig. 6. The dependence of the frequency of El Niño on the dynamical coupling strength between the atmosphere and ocean (α). Same as in Fig. 2, the frequency of El Niño is measured here by the return period. Note that the shorter the return period, the higher the frequency. The dots marked by a, b, c, d, e, and f correspond respectively to the time series shown in Fig. 7a, Fig. 7b, Fig. 7c, Fig. 7d, Fig. 7e, and Fig. 7f. The black dots indicate the regime that has a single-loop limit cycle, while the red dots correspond to the regime where the oscillations result from two-loop or multi-loop limit cycles. Inside the shaded area are steady regimes with no oscillations. While varying the value of α, T_e, $1/c$, s, and $1/r$ are fixed respectively to 31.00°C, 150 days, 0.096, and 300 days. $\alpha_0 / a = 3.0 \times 10^{-8}$ K^{-1} s^{-1}. Other parameters are kept the same as those in Sun (1997).

As we have found with increasing the intensity of radiative heating (T_e), increasing the dynamical coupling strength between the atmosphere and ocean (α) can also lead to more frequent El Niño events (Fig. 6). The range of α within which the system can generate oscillations spans from $0.74\,\alpha_0$ to $1015\,\alpha_0$. In this range, the dependence of frequency on α is strongly nonlinear. There are distinct dynamic regimes, with the dependence of frequency on α varying across these regimes. The regime where the system is in further depends on the value of α. As shown in the figure, the system experiences three dynamic regimes. Over a wide range of α (smaller than $0.96\,\alpha_0$), there is a slow increase in the frequency as α increase, with the system oscillating periodically (first black segment). Once α exceeds a critical value ($0.97\,\alpha_0$), the increase in frequency becomes more pronounced, transitioning

into the regime where the growth accelerates significantly. In this regime, the system exhibits oscillations with two or more different magnitudes (shown by the red dots). As α continues to increase (α exceeds α_0), the system enters a regime where the rate of increase in frequency becomes even faster (second black segment). Sun (1997) used 3.0×10^{-8} K^{-1} s^{-1} as an estimate for α/a based on ballpark calculations of the zonal wind-stress sensitivity to the zonal SST contrast and Rayleigh damping.

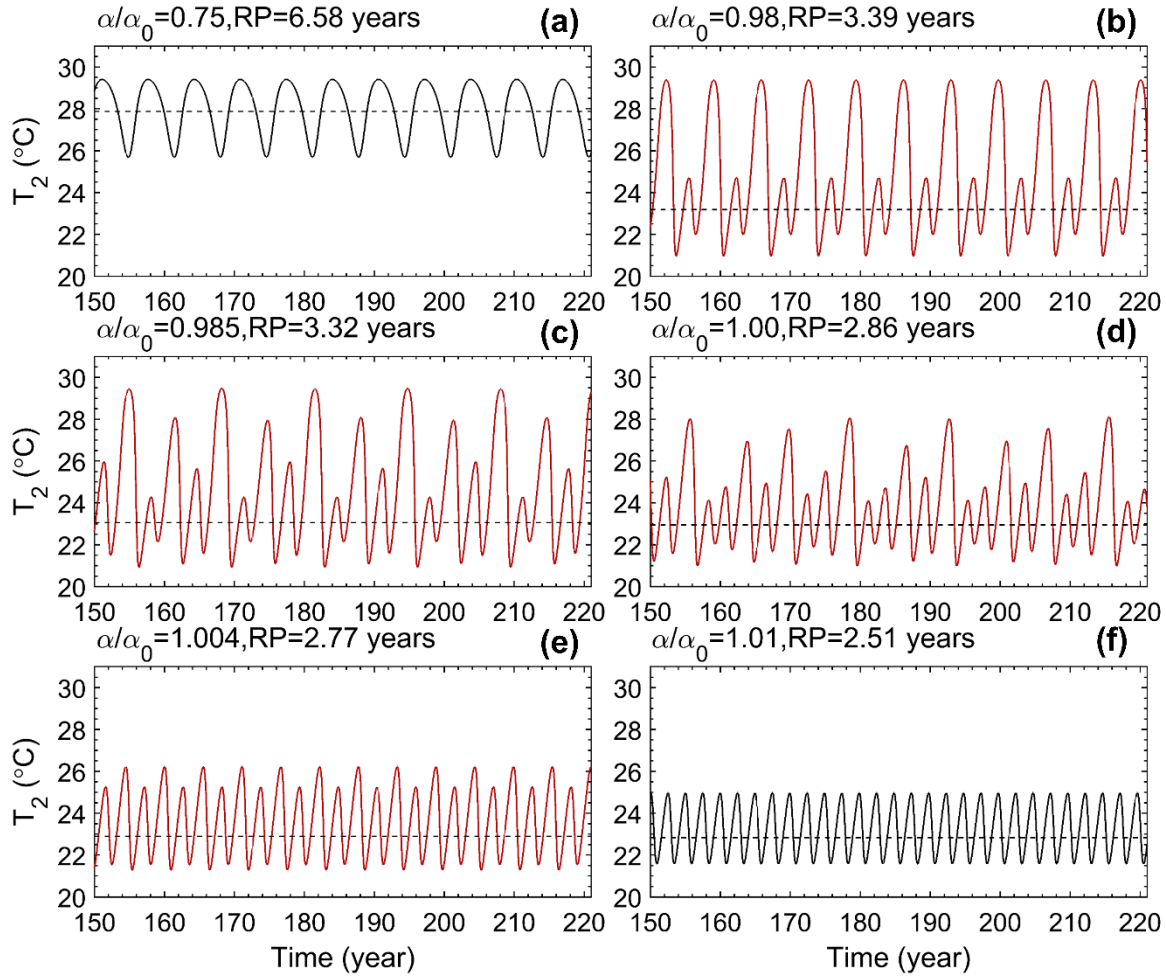

Fig. 7. Time series of eastern equatorial Pacific SST (T_2) under varying values of dynamical coupling strength between the atmosphere and ocean (α). The corresponding values of the return period (RP) of El Niño events are indicated at the top of the time series. The time series shown in Fig. 7a, Fig. 7b, Fig. 7c, Fig. 7d, Fig. 7e, and Fig. 7f are taken from the dots marked a, b, c, d, e, and f in Fig. 6, respectively. Time series corresponding to a single-loop limit cycle are shown in black, while those corresponding to two or more loop limit cycles are shown in red. The dashed line corresponds to the equilibrium value of T_2.

The characteristics of the time series corresponding to different dynamic regimes, identified by varying the values of α, closely resemble those of the time series obtained by varying the

387 value of T_e (Fig. 7). When α is small (Fig. 7a), the system exhibits an oscillatory pattern with
388 a single magnitude. As the value of α increases, the system transitions into a regime
389 characterized by oscillations with two or more magnitudes of El Niño events, accompanied by
390 more frequent (shorter return period) El Niño events. Finally, when α exceeds $1.01\alpha_0$ (Fig.
391 7f), the oscillatory pattern reverts to a single magnitude but with a much shorter return period.

392 When varying T_e and α, the dynamical behavior of the system exhibits remarkable
393 similarity. This similarity may be attributed to the fact that the system's behavior is
394 fundamentally governed by a set of non-dimensional parameters. Sun (1997) identified four
395 non-dimensional parameters— R, Λ, δ, and s —that determine the system's dynamical
396 behavior. Among these, $R\,(=\frac{\alpha(T_e - T_{s0})}{ac})$ is the most important, as it measures the strength of
397 thermal forcing relative to thermal damping and mechanical dissipation within the coupled
398 system. Importantly, the system's thermal forcing is determined by both T_e and α, which
399 explains why variations in these two parameters lead to similar dynamical behaviors.

400 *c. The dependence of El Niño frequency on the strength of zonal advection*

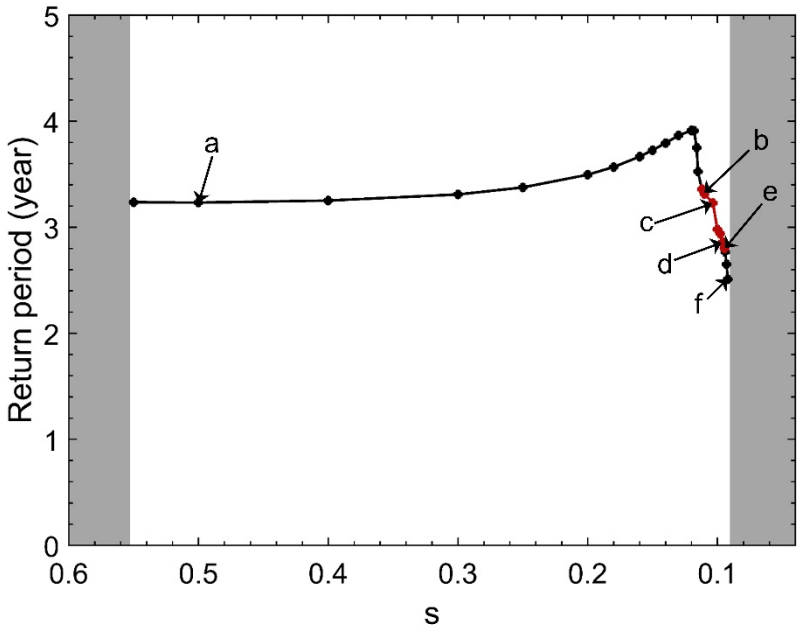

401

402 Fig. 8. The dependence of the frequency of El Niño on the strength of zonal advection
403 (relative to the total upwelling) s. The dots labeled a, b, c, d, e, and f correspond to where the
404 time series shown in Fig. 9a, Fig. 9b, Fig. 9c, Fig. 9d, Fig. 9e, and Fig. 9f are taken, respectively.
405 Black dots indicate regimes with a single-loop limit cycle, while red dots indicate regimes with
406 two-loop or multi-loop limit cycles. The shaded area denotes steady regimes with no

oscillations. While varying the value of s, T_e, α/a, $1/c$ and $1/r$ are fixed respectively to 31.00°C, 3.0×10^{-8} K^{-1} s^{-1}, 150 days , and 300 days. Other parameters are adopted as in Sun (1997). Note that s decreases from the left to the right.

Overall, the frequency of El Niño varies nonlinearly with changes in the strength of zonal advection (s). The system can generate oscillations when the value of s lies between 0.092 and 0.55. For s >0.12, the frequency changes slowly with s; however, for s <0.12, the frequency increases abruptly as s decreases. Based on simulations from a GCM (Timmermann et al. 1999), Timmermann et al. (2003) estimated that the range of s in the present climate is approximately 0.04–0.1. Figure 8 shows that within this range, the frequency of El Niño increases as s decreases. This reduction in s leads to a decrease in the zonal SST contrast, creating conditions more conducive to El Niño development.

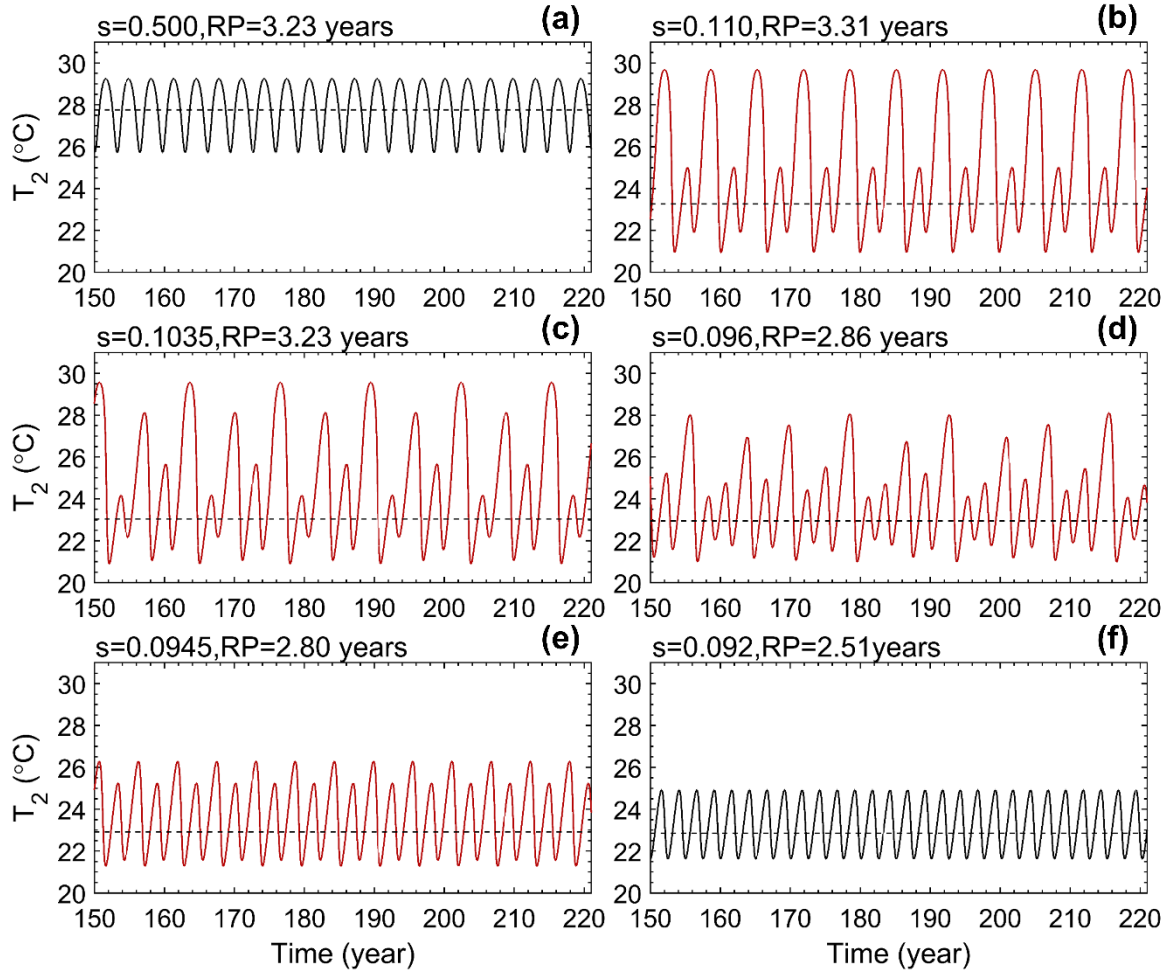

Fig. 9. Time series of eastern equatorial Pacific SST (T_2) under different values of zonal advection (s). The corresponding values of the return period (RP) of El Niño events are indicated at the top of the time series. The time series shown in Fig. 9a, Fig. 9b, Fig. 9c, Fig. 9d, Fig. 9e, and Fig. 9f correspond to the dots marked a, b, c, d, e, and f in Fig. 8. The time

series with two or more different El Niño magnitudes are plotted in a different color (red). The dashed line corresponds to the equilibrium value of T_2.

The characteristics of the time series of T_2 corresponding to single magnitude, two or more magnitudes are all found by varying the value of s (Fig. 9). Liang et al. (2017) identified that when s >0.12, ENSO asymmetry exhibits a negative value, which is inconsistent with observations. Therefore, we focus on the range where s <0.12. The results further demonstrate that the model exhibits multiple dynamic regimes with different oscillation patterns, and changes in these oscillation patterns alter the frequency of El Niño events.

d. The dependence of El Niño frequency on the thermal damping coefficient

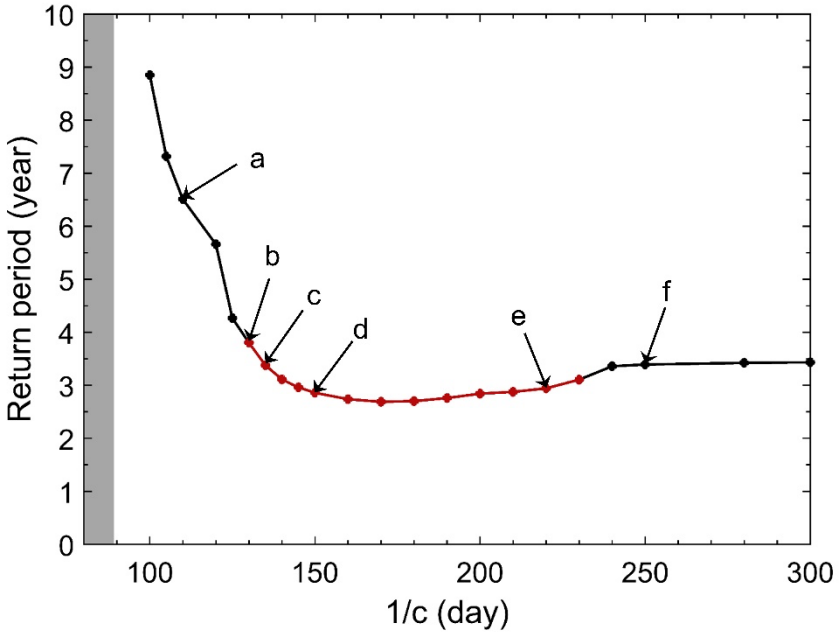

Fig. 10. The dependence of the frequency of El Niño on the thermal damping coefficient (c). The dots marked by a, b, c, d, e, and f are where the time series shown in Fig. 11a, Fig. 11b, Fig. 11c, Fig. 11d, Fig. 11e, and Fig. 11f are taken, respectively. The black dots indicate the regimes with a single-loop limit cycle, while the red dots indicate the regimes where the oscillations result from a two-loop or a multi-loop limit cycle. The shaded area are steady regimes with no oscillations. While varying the value of c, T_e, α/a, s, and $1/r$ are fixed respectively to 31.00℃, 3.0×10^{-8} K^{-1} s^{-1}, 0.096, and 300 days. Other parameters are kept the same as those in Sun (1997).

More frequent El Niño events can be produced with a longer time-scale of thermal damping from the atmosphere ($1/c$). When the value of $1/c$ is greater than 90days, the system can generate oscillations. As with other parameters discussed before, the dependence of frequency on $1/c$ is nonlinear also. The system transitions through different dynamic regimes as the value

of $1/c$ changes. When $1/c$ is small (roughly from 90 to 160 days), the system is in the regime where the frequency increases with $1/c$. The longer the time-scale of thermal damping (larger $1/c$), the more time the surface flux takes to dampen an SST anomaly, leading to more frequent El Niño events. This is consistent with early analysis of El Niño (Sun 2000), as an increase in $1/c$ leads to an increase in the non-dimensional parameter $\sigma\,(=r/c)$, which determines the system's behavior. While as $1/c$ exceeds 160 days, the system enters a dynamic regime where the frequency becomes nearly constant. The value of $1/c$ used in the literature ranges from 150 to 200 days (Jin 1996; Sun 1997, 2003; Timmermann and Jin 2002; Timmermann et al. 2003).

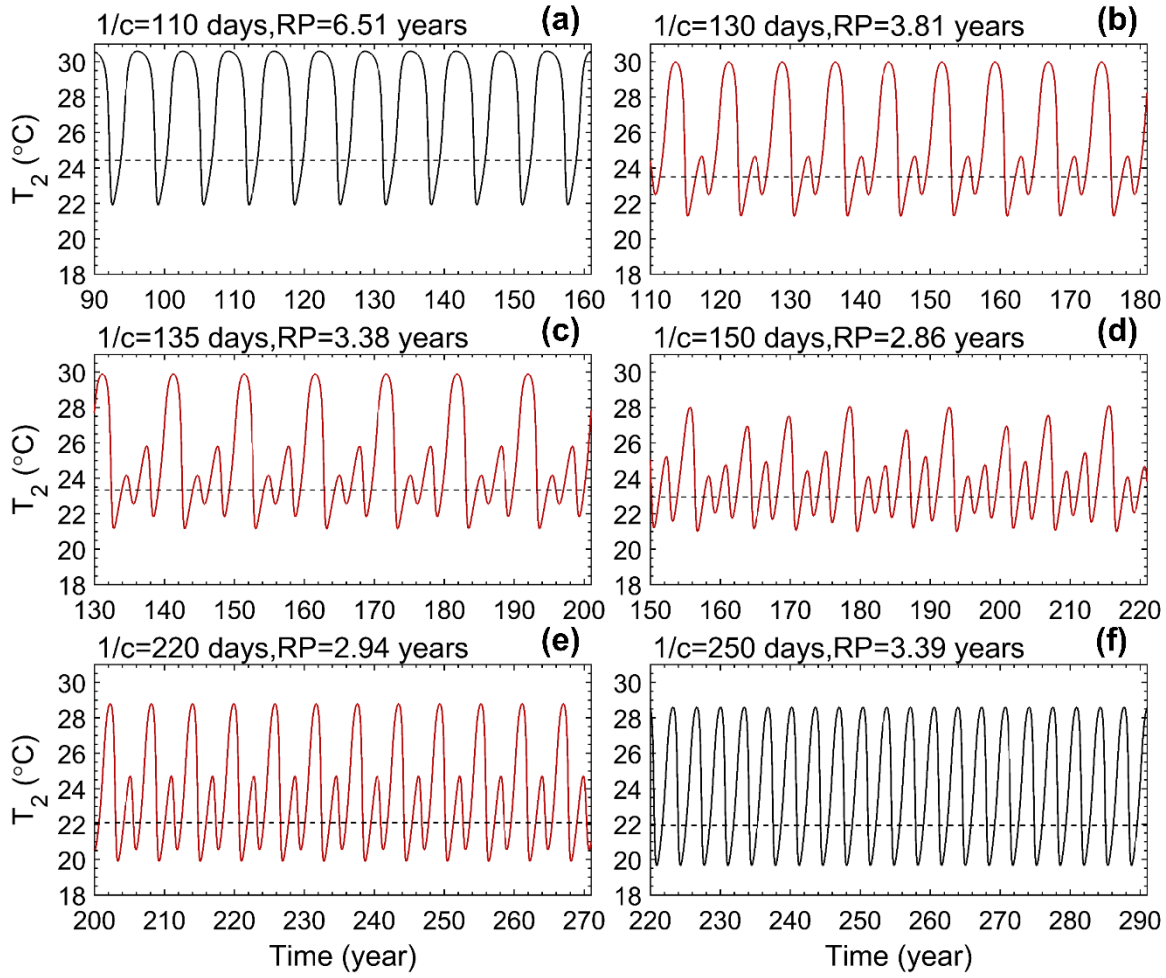

Fig. 11. Time series of eastern equatorial Pacific SST (T_2) corresponding to different values of the thermal damping coefficient (c). The corresponding values of the return period (RP) of El Niño events are indicated at the top of the time series. The time series shown in Fig. 11a, Fig. 11b, Fig. 11c, Fig. 11d, Fig. 11e, and Fig. 11f correspond to the dots marked by a, b, c, d, e, and f in Fig. 10. Time series with a single magnitude of El Niño are shown in black, while

time series with two or more different magnitudes are shown in red. The dashed line corresponds to the equilibrium value of T_2.

As $1/c$ increases, we once again find that the system exhibits multiple oscillation patterns, including periodic oscillations, oscillations with two magnitudes, and oscillations with multiple magnitudes. The specific pattern of oscillation depends on the regime the system finds itself in, which is further determined by the value of $1/c$. Note during the regime where the frequency of El Niño increases with $1/c$, the oscillatory behavior transitions sequentially from single magnitude to two magnitudes, then to three magnitudes, and finally to multiple magnitudes.

e. The dependence of El Niño frequency on the dynamical adjustment time-scale for the upper ocean

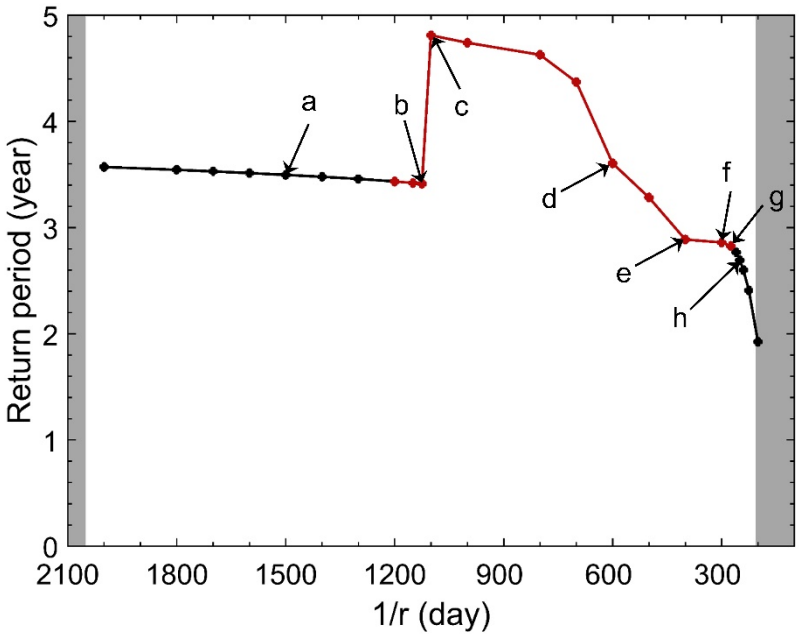

Fig. 12. The dependence of the frequency of El Niño on the parameter that measures the upper ocean memory (r). The dots marked a, b, c, d, e, f, g, and h correspond to the cases whose time series are presented in Fig. 13a, Fig. 13b, Fig. 13c, Fig. 13d, Fig. 13e, Fig. 13f, Fig. 13g, and Fig. 13h, respectively. The black dots represent the regimes with a single-loop limit cycle, while the red dots indicate the regimes with two-loop or multi-loop limit cycles. The shaded area represents steady regimes with no oscillations. While varying the value of r, T_e, α/a, $1/c$, and s are fixed respectively to 31.0°C, 3.0×10^{-8} K^{-1} s^{-1}, 150 days, and 0.096. The values of the other parameters follow those given in Sun (1997). Note that $1/r$ is in decreasing order from the left to the right.

More frequent El Niño events can also result from a faster response of the equatorial upper ocean to wind forcing (or from the "leaking rate" of water in the upper equatorial western

Pacific, as the two are considered equivalent here) (Fig. 12). The values of $1/r$ for the system generate oscillation range from 200 days to 2050 days. The frequency of El Niño exhibits a nonlinear relationship with changes in $1/r$. However, over a significant range of $1/r$, the return period decreases as $1/r$ decreases (i.e., the frequency increases as $1/r$ decreases). Note $1/r$ corresponds to the delay time of the negative feedback in the delayed oscillator theory (Battisti 1988; Suarez and Schopf 1988). Within this specific range, the findings support the conclusions of the delayed oscillator theory. However, when the value of $1/r$ exceeds 1100 days—an unrealistic value—the frequency of El Niño events remains nearly constant as $1/r$ increases (even in this regime, the frequency still decreases, albeit very slowly, with $1/r$). Unlike the delayed oscillator theory, the model we use is nonlinear and involves other physical processes that collectively determine the frequency of El Niño through their combined impact on the stability of the system. Values for $1/r$ used in the literature range from 300 to 400 days (Jin 1996; Timmermann and Jin 2002; Timmermann et al. 2003).

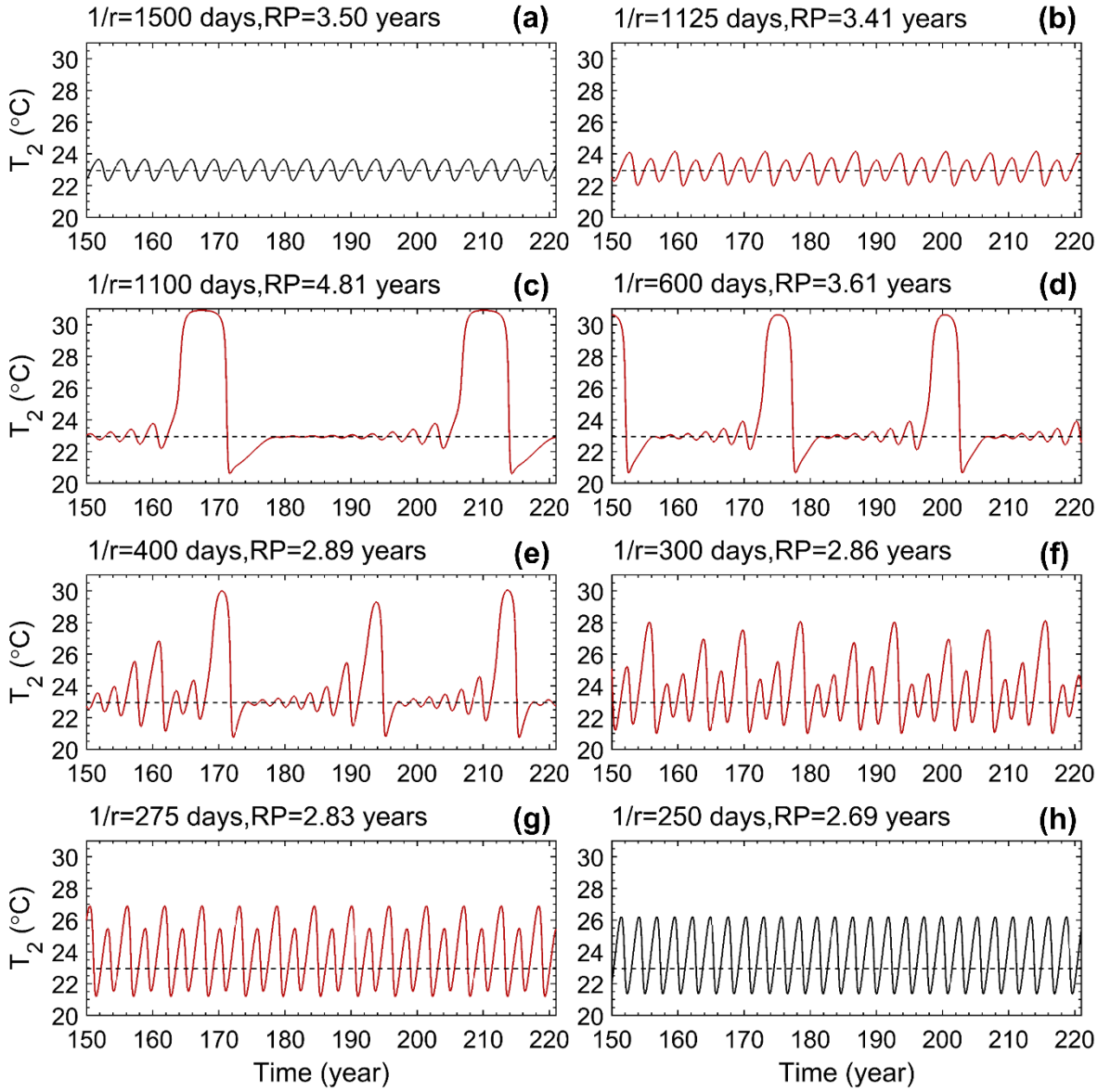

Fig. 13. Time series of eastern equatorial Pacific SST (T_2) under different values of parameter that measures the upper ocean memory (r). The corresponding values of the return period (RP) of El Niño events are indicated at the top of the time series. The time series shown in Fig. 13a, Fig. 13b, Fig. 13c, Fig. 13d, Fig. 13e, Fig. 13f, Fig. 13g, and Fig. 13h correspond to the dots marked by a, b, c, d, e, f, g, and h in Fig. 12. A different color (red) is used in plotting the time series that have a varying El Niño magnitude. The dashed line corresponds to the equilibrium value of T_2.

As $1/r$ changes, the system also exhibits different oscillation patterns, with each oscillation pattern corresponding to a different El Niño frequency. We particularly note that when the frequency of El Niño events undergoes a significant change (Fig. 12), the oscillation pattern in the time series also shifts noticeably. Specifically, when $1/r$ changes from 1125 days to 1100 days (Fig. 13b and 13c), there is a clear transition in the oscillation pattern: the system shifts

from a relatively weak El Niño state to one characterized by the sudden burst of a very strong El Niño event. This finding further emphasizes the sensitivity of nonlinear systems to parameter changes, where even a slight variation can lead to a dramatic shift in the system's behavior.

4. Summary and discussion

Motivated to better understand the physical processes that may be important in determining the frequency of El Niño events, particularly the role of the intensity of radiative heating, we have employed the simple nonlinear model of El Niño developed by Sun (1997)—a model that has been shown to capture a broad range of observed major characteristics of El Niño including its asymmetry with La Niña and its decadal changes (Timmermann and Jin 2002; Kim and An 2011; Liang et al. 2012; Roberts et al. 2016; Guckenheimer et al. 2017; Kohyama and Hartmann 2017; Liang et al. 2017; Ray et al. 2020). Notably, even the most sophisticated models—the CMIP6 models—continue to struggle with simulating the ENSO asymmetry (Hayashi et al. 2020; Planton et al. 2021; Zhao and Sun 2022), underscoring a unique strength of this model. Despite its high capacity, the model is a box model that only has three predictive equations, allowing sensitivity experiments to be conducted very efficiently, especially when the physical parameters need to be varied over a wide range.

The results from a suite of sensitivity experiments with this model show that the frequency of El Niño events depends on multiple parameters, including the intensity of radiative heating as measured by the radiative-convective equilibrium SST. The traditionally emphasized time-scale for the equatorial ocean to equilibrate with the surface winds—the upper ocean memory—is just one of many factors influencing the frequency of El Niño. In analogy to a symphony, where a melody is composed of sounds from multiple instruments, the tune of El Niño arises from the interplay of multiple physical processes.

A fundamental mechanism by which the intensity of radiative heating affects the frequency of El Niño events is its impact on the generation of increasingly complex limit cycles by the system, which in turn alters oscillation patterns. The results highlight an aspect of the ENSO system that has been largely overlooked in determining how frequently El Niño takes place. Proper accounting of nonlinearity in the ENSO system brings the role of the intensity of radiative heating to the forefront. Another factor in the model of Sun (1997) that helps to emphasize the role of the intensity of radiative heating is that the model is not an anomaly one,

and the subsurface "feels" the intensity of radiative heating, albeit in an empirical and highly simplified way. In models with a fixed climatology for the surface and subsurface, the role of radiative heating is hidden in the prescribed climatology (or the mean state).

Other parameters—the dynamical coupling strength between the atmosphere and ocean, the strength of zonal advection relative to upwelling, the thermal damping coefficient from the atmosphere, and the dynamical adjustment time-scale for the upper ocean are found to affect the frequency of El Niño in a similar way to the intensity of radiative heating: their changes induce regime changes, and thereby alter oscillation patterns. Sensitivity experiments with these parameters help to gauge the importance of the intensity of radiative heating. Like the experiments on the role of the intensity of radiative heating, these experiments also highlight the critical importance of nonlinearity in influencing the frequency of El Niño.

In addition to providing a pedagogical exercise to highlight the roles of physical processes that have not been as emphasized as the dynamical adjustment time-scale for the upper ocean in determining El Niño frequency—and more generally, the fundamental role of nonlinearity—our results may also contribute to understanding the sources of biases in ENSO simulations by fully coupled GCMs. Both radiative heating and the thermal damping coefficient are closely linked to cloud feedback (Sun and Liu 1996), and our analysis of El Niño frequency sensitivity to these two factors offers a promising avenue for further exploration into the role of cloud feedback in ENSO simulations. Indeed, fully coupled GCMs exhibit substantial biases in simulating cloud feedback (Sun et al. 2006; Sun et al. 2009; Bellenger et al. 2014; Ying and Huang 2016), which will lead to inaccuracies in radiative heating and thermal damping coefficient values, subsequently leading to biases in El Niño frequency simulations. Additionally, previous studies have demonstrated that GCMs significantly underestimate the strength of ocean-atmosphere coupling (Sun et al. 2016; Bayr et al. 2020; Hayashi et al. 2020; Wang et al. 2021; Zhao and Sun 2022), while overestimating the strength of zonal advection (Sun et al. 2003; Sun et al. 2006; Zheng et al. 2012; Sun et al. 2013; Li and Xie 2014; Zhang and Sun 2014; Li et al. 2016; Sun et al. 2016; Li et al. 2019; Jiang et al. 2021), all of which may significantly affect ENSO simulations, as implied by the results from the present study.

Moreover, the role of nonlinearity and the regime changes it supports in determining the frequency of El Niño events, as evident in this simple yet highly capable box model, suggests that an inherently nonlinear framework may be necessary for diagnosing the causes of biases in the most sophisticated climate models, such as the CMIP6 models. By an inherently

570 nonlinear framework, we mean that we need to rely on the "regimes" discerned from models
571 and observations and what they imply—rather than solely on heat budget studies that include
572 contributions from the nonlinear terms in the heat budget equations to the initial growth rate.
573 The sensitivity studies reported here should help identify the key parameters that determine
574 which regime a GCM is in, and accordingly help to understand the causes for the diversity of
575 ENSO among these models and their differences from observations.

576 The results reported here—particularly those concerning the role of radiative heating
577 intensity—are also expected to help explain changes in El Niño frequency observed in both
578 historical records and climate model simulations. A specific application of the present
579 theoretical findings to interpret these changes, including those reported under global warming
580 scenarios, will be presented in a separate study, drawing on the mechanism identified here
581 through which radiative heating intensity influences El Niño frequency.

582 Finally, we caution that the results are from a simple model. It is capable of complex
583 behavior, reminiscent of the complex behavior of El Niño events in the observations, but
584 nonetheless, it is a highly simplified model. The full utility of such a model can only be realized
585 when it is used in close conjunction with more comprehensive models, such as the NCAR
586 CESM. The role of random forcing from weather events needs to be investigated. In addition,
587 to underscore the origin of El Niño and illuminate its nonlinear dynamics, we have used an
588 excursion of the system from its equilibrium state towards a warmer situation (measured by the
589 eastern equatorial Pacific SST) to define an El Niño event in this study. Future studies need to
590 examine the impact of using the traditional way to identify an El Niño event—defined by a
591 positive anomaly relative to the climatology—on the results. Alternatively, we can also identify
592 El Niño events in the observations in the same way as we have used in this model. Accurately
593 estimating equilibrium states for the coupled tropical Pacific ocean-atmosphere system may be
594 difficult, but it is not impossible.

595

596 *Acknowledgments.*

597 Z.G. appreciates the technical help from Dr. Jin Liang in the initial state of this research.
598 We would also like to thank the reviewers and the editor for their very helpful comments and
599 suggestions. This research was supported by the National Natural Science Foundation of China
600 under grant 42250710154.

Data Availability Statement.

The data used in this study is available at https://zenodo.org/records/15351819.

APPENDIX A

El Niño Model of Sun (1997)

Figure A1 is a schematic diagram for the box model of Sun (1997).

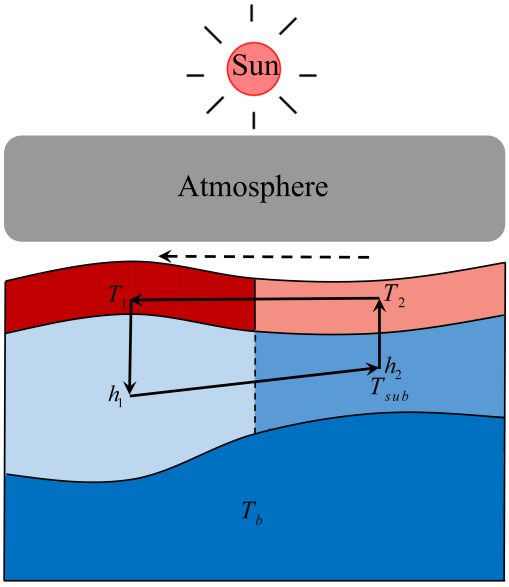

Fig. A1. A schematic diagram for the coupled model of Sun (1997). Solid arrows in black represent the zonal branch of the equatorial wind-driven circulation constituted by the upwelling in the east Pacific, the westward surface drift, and the equatorial undercurrent. The dashed arrow represents the surface winds. The model consists of five boxes: two for the surface ocean—representing the surface western and the surface eastern equatorial Pacific, respectively; two for the two corresponding subsurface upper ocean; and one for the deep ocean. The depths h_1 and h_2 represent the thermocline depths in the western and eastern equatorial Pacific, respectively.

The model equations are as follows:

$$\frac{dT_1}{dt} = c(T_e - T_1) + sq(T_2 - T_1), \tag{A1}$$

$$\frac{dT_2}{dt} = c(T_e - T_2) + q(T_{sub} - T_2), \tag{A2}$$

$$q = \frac{\alpha}{a}(T_1 - T_2), \tag{A3}$$

$$T_{sub} = \Phi(-H_1 + h_2'), \tag{A4}$$

$$\Phi(z) = T_e - \frac{T_e - T_b}{2}\left[1 - \tanh\left(\frac{z + z_0}{H^*}\right)\right], \tag{A5}$$

$$h_2' - h_1' = -\frac{H_1}{H_2} H \frac{\alpha}{b^2}(T_1 - T_2), \text{ and} \tag{A6}$$

$$\frac{dh_1'}{dt} = -rh_1' + r\frac{H_1}{2H_2} H \frac{\alpha}{b^2}(T_1 - T_2). \tag{A7}$$

Eqs. (A1)–(A2) and (A7) are the three predictive equations of this system. Eq. (A1) is for western equatorial Pacific SST (T_1), Eq. (A2) is for the eastern (T_2) equatorial Pacific SST, and Eq. (A7) is for the thermocline depth in the western Pacific (h_1') relative to a fixed reference value for the zonal mean depth H ($h_1' = h_1 - H$). The two terms on the right hand of Eqs. (A1) and (A2) are respectively the local heat flux into the ocean and the effect of advection by ocean currents. T_e is the radiative-convective equilibrium temperature; $1/c$ is the time-scale for the atmospheric processes to remove a SST anomaly. $q = w/H_1$, where w represents the strength of upwelling in the eastern equatorial Pacific and H_1 is the depth of the surface layer. Assuming that the strength of the ocean current is proportional to the zonal wind-stress, which in turn is proportional to the zonal SST contrast, we have Eq. (A3) where α measures the sensitivity of the zonal wind stress to the zonal SST contrast between the eastern and western tropical Pacific, and a defines the adjustment time-scale of the ocean currents to a change in the surface winds. Zonal advection—the amount of water flowing from the eastern tropical Pacific to the western tropical Pacific—is assumed to be a fraction of the total upwelling in the eastern tropical Pacific and this fraction is measured by s. T_{sub} is the temperature of water upwelled to the surface ocean from the subsurface ocean, and is linked to the depth of the thermocline in the eastern tropical Pacific relative to H ($h_2' = h_2 - H$) (Eq. A4) and a prescribed vertical profile for the temperature across the thermocline (Eq. A5). The contrast between thermocline depth in the equatorial western Pacific ($h_1' = h_1 - H$) and that in the eastern equatorial Pacific ($h_2' = h_2 - H$) is assumed to be proportional to the zonal wind stress as shown in Eq. (A6). Eq. (A7) shows that the time evolution of the thermocline depth in the western equatorial Pacific is determined by two terms: the second term on the right-hand side represents

646 the “filling” due to the “piling up” caused by the zonal wind, which is proportional to the zonal
647 SST contrast; the first term on the right-hand side of the equation represents the rate of
648 “leaking”, which is linearly proportional to the depth of the thermocline—the more warm water
649 accumulated in the western Pacific due to the piling effect of the surface wind, the greater the
650 rate of “loss” of water owing to other processes. The time-scale of the “leaking” is assumed to
651 be the same as the time-scale for the adjustment of the equatorial upper ocean to a change in
652 the surface winds, and this time-scale is measured here by $1/r$. More detailed description of
653 these equations and parameters can be found in Sun (1997).

654

655 REFERENCES

656 An, S.-I., and B. Wang, 2000: Interdecadal change of the structure of the ENSO mode and its
657 impact on the ENSO frequency. *J. Clim.*, **13,** 2044-2055.

658 Arblaster, J. M., and L. V. Alexander, 2012: The impact of the El Niño-Southern Oscillation
659 on maximum temperature extremes. *Geophys. Res. Lett.*, **39**.

660 Battisti, D. S., 1988: Dynamics and Thermodynamics of a Warming Event in a Coupled
661 Tropical Atmosphere–Ocean Model. *J. Atmos. Sci.*, **45,** 2889-2919.

662 Bayr, T., D. Dommenget, and M. Latif, 2020: Walker circulation controls ENSO atmospheric
663 feedbacks in uncoupled and coupled climate model simulations. *Clim. Dyn.*, **54,** 2831-2846.

664 Bellenger, H., É. Guilyardi, J. Leloup, M. Lengaigne, and J. Vialard, 2014: ENSO
665 representation in climate models: From CMIP3 to CMIP5. *Clim. Dyn.*, **42,** 1999-2018.

666 Cai, W., G. Wang, A. Santoso, X. Lin, and L. Wu, 2017: Definition of extreme El Niño and its
667 impact on projected increase in extreme El Niño frequency. *Geophys. Res. Lett.*, **44,** 11,184-
668 111,190.

669 Cai, W., and Coauthors, 2014: Increasing frequency of extreme El Niño events due to
670 greenhouse warming. *Nat. Clim. Change*, **4,** 111-116.

671 Cai, W., and Coauthors, 2021: Changing El Niño–Southern Oscillation in a warming climate.
672 *Nat. Rev. Earth Environ.,* **2**, 628–644.

673 Capotondi, A., and P. D. Sardeshmukh, 2017: Is El Niño really changing? *Geophys. Res. Lett.*,
674 **44,** 8548-8556.

675 Capotondi, A., C. Deser, A. Phillips, Y. Okumura, and S. Larson, 2020: ENSO and Pacific
676 decadal variability in the Community Earth System Model version 2. *J. Adv. Model. Earth*
677 *Syst.*, **12,** e2019MS002022.

678 Chang, P., B. Wang, T. Li, and L. Ji, 1994: Interactions between the seasonal cycle and the
679 Southern Oscillation-Frequency entrainment and chaos in a coupled ocean-atmosphere
680 model. *Geophys. Res. Lett.*, **21,** 2817-2820.

681 Deng, L., X. Yang, and Q. Xie, 2010: ENSO frequency change in coupled climate models as
682 response to the increasing CO_2 concentration. *Chin. Sci. Bull.*, **55,** 744-751.

683 Deser, C., and Coauthors, 2012: ENSO and Pacific decadal variability in the Community
684 Climate System Model version 4. *J. Clim.*, **25,** 2622-2651.

685 Eyring, V., S. Bony, G. A. Meehl, C. A. Senior, B. Stevens, R. J. Stouffer, and K. E. Taylor,
686 2016: Overview of the Coupled Model Intercomparison Project Phase 6 (CMIP6)
687 experimental design and organization. *Geosci. Model Dev.*, **9,** 1937-1958.

688 Fedorov, A. V., and S. G. Philander, 2000: Is El Niño changing? *Science*, **288,** 1997-2002.

689 Fredriksen, H. B., J. Berner, A. C. Subramanian, and A. Capotondi, 2020: How does El Niño–
690 Southern Oscillation change under global warming—A first look at CMIP6. *Geophys. Res.*
691 *Lett.*, **47,** e2020GL090640.

692 Gao, T., M. Luo, N. C. Lau, and T. Chan, 2020: Spatially distinct effects of two El Niño types
693 on summer heat extremes in China. *Geophys. Res. Lett.*, **47,** e2020GL086982.

694 Guckenheimer, J., A. Timmermann, H. Dijkstra, and A. Roberts, 2017: (Un) predictability of
695 strong El Niño events. *Dynamics Statistics of the Climate System*, **2,** dzx004.

696 Hayashi, M., F.-F. Jin, and M. F. Stuecker, 2020: Dynamics for El Niño-La Niña asymmetry
697 constrain equatorial-Pacific warming pattern. *Nat. Commun.*, **11,** 4330.

698 Held, I. M., 2005: The gap between simulation and understanding in climate modeling. *Bull.*
699 *Am. Meteorol. Soc.*, **86,** 1609-1614.

700 Hirahara, S., M. Ishii, and Y. Fukuda, 2014: Centennial-scale sea surface temperature analysis
701 and its uncertainty. *J. Clim.*, **27,** 57-75.

702 Hu, Z.-Z., A. Kumar, B. Huang, J. Zhu, and H.-L. Ren, 2017a: Interdecadal variations of ENSO
703 around 1999/2000. *J. Meteorolog. Res.*, **31,** 73-81.

Hu, Z.-Z., A. Kumar, H.-L. Ren, H. Wang, M. L'Heureux, and F.-F. Jin, 2013: Weakened interannual variability in the tropical Pacific Ocean since 2000. *J. Clim.*, **26,** 2601-2613.

Hu, Z.-Z., A. Kumar, J. Zhu, B. Huang, Y.-h. Tseng, and X. Wang, 2017b: On the shortening of the lead time of ocean warm water volume to ENSO SST since 2000. *Sci. Rep.*, **7,** 1-7.

Hua, L., D.-Z. Sun, and Y. Yu, 2019: Why do we have El Niño: Quantifying a diabatic and nonlinear perspective using observations. *Clim. Dyn.*, **52,** 6705-6717.

Huang, B., and Coauthors, 2017: Extended reconstructed sea surface temperature, version 5 (ERSSTv5): upgrades, validations, and intercomparisons. *J. Clim.*, **30,** 8179-8205.

Jiang, W., P. Huang, G. Huang, and J. Ying, 2021: Origins of the excessive westward extension of ENSO SST simulated in CMIP5 and CMIP6 models. *J. Clim.*, **34,** 2839-2851.

Jin, F.-F., J. D. Neelin, and M. Ghil, 1994: El Niño on the devil's staircase: Annual subharmonic steps to chaos. *Science*, **264,** 70-72.

Jin, F.-F., 1996: Tropical ocean-atmosphere interaction, the Pacific cold tongue, and the El Niño-Southern Oscillation. *Science*, **274,** 76-78.

Kim, B.-M., and S.-I. An, 2011: Understanding ENSO regime behavior upon an increase in the warm-pool temperature using a simple ENSO model. *J. Clim.*, **24,** 1438-1450.

Kleeman, R., 2008: Stochastic theories for the irregularity of ENSO. *Philosophical Transactions of the Royal Society A: Mathematical, Physical and Engineering Sciences*, **366,** 2509-2524.

Kohyama, T., and D. L. Hartmann, 2017: Nonlinear ENSO warming suppression (NEWS). *J. Clim.*, **30,** 4227-4251.

Li, G., and S.-P. Xie, 2014: Tropical biases in CMIP5 multimodel ensemble: The excessive equatorial Pacific cold tongue and double ITCZ problems. *J. Clim.*, **27,** 1765-1780.

Li, G., S.-P. Xie, Y. Du, and Y. Luo, 2016: Effects of excessive equatorial cold tongue bias on the projections of tropical Pacific climate change. Part I: The warming pattern in CMIP5 multi-model ensemble. *Clim. Dyn.*, **47,** 3817-3831.

Li, G., and Coauthors, 2019: Effect of excessive equatorial Pacific cold tongue bias on the El Niño-Northwest Pacific summer monsoon relationship in CMIP5 multi-model ensemble. *Clim. Dyn.*, **52,** 6195-6212.

Liang, J., X.-Q. Yang, and D.-Z. Sun, 2012: The effect of ENSO events on the tropical Pacific mean climate: Insights from an analytical model. *J. Clim.*, **25,** 7590-7606.

——, 2017: Factors determining the asymmetry of ENSO. *J. Clim.*, **30,** 6097-6106.

Lorenz, E. N., 1963: Deterministic Nonperiodic Flow. *J. Atmos. Sci.*, **20,** 130-141.

McPhaden, M. J., 2012: A 21st century shift in the relationship between ENSO SST and warm water volume anomalies. *Geophys. Res. Lett.*, **39**.

Pathirana, G., and Coauthors, 2023: Increase in convective extreme El Niño events in a CO2 removal scenario. *Sci. Adv.*, **9,** eadh2412.

Penland, C., 1996: A stochastic model of IndoPacific sea surface temperature anomalies. *Physica D*, **98,** 534-558.

——, and P. D. Sardeshmukh, 1995: The optimal growth of tropical sea surface temperature anomalies. *J. Clim.*, **8,** 1999-2024.

Picaut, J., F. Masia, and Y. Du Penhoat, 1997: An advective-reflective conceptual model for the oscillatory nature of the ENSO. *Science*, **277,** 663-666.

Planton, Y. Y., and Coauthors, 2021: Evaluating climate models with the CLIVAR 2020 ENSO metrics package. *Bull. Am. Meteorol. Soc.*, **102,** E193-E217.

Ray, A., S. Rakshit, G. K. Basak, S. K. Dana, and D. Ghosh, 2020: Understanding the origin of extreme events in El Niño southern oscillation. *Phys. Rev. E*, **101,** 062210.

Rayner, N., and Coauthors, 2003: Global analyses of sea surface temperature, sea ice, and night marine air temperature since the late nineteenth century. *J. Geophys. Res.: Atmos.*, **108,** 4407.

Roberts, A., J. Guckenheimer, E. Widiasih, A. Timmermann, and C. K. Jones, 2016: Mixed-mode oscillations of El Niño–Southern Oscillation. *J. Atmos. Sci.*, **73,** 1755-1766.

Rodríguez-Morata, C., H. Díaz, J. A. Ballesteros-Canovas, M. Rohrer, and M. Stoffel, 2019: The anomalous 2017 coastal El Niño event in Peru. *Clim. Dyn.*, **52,** 5605-5622.

Shin, N.-Y., J.-S. Kug, M. F. Stuecker, F.-F. Jin, A. Timmermann, and G.-I. J. n. C. Kim, 2022: More frequent central Pacific El Niño and stronger eastern pacific El Niño in a warmer climate. *NPJ Clim. Atmos. Sci.*, **5,** 101.

761 Strogatz, S. H., 2015: *Nonlinear dynamics and chaos: With applications to physics, biology,*
762 *chemistry, and engineering* (2nd ed.). CRC press.

763 Suarez, M. J., and P. S. Schopf, 1988: A delayed action oscillator for ENSO. *J. Atmos. Sci.*, **45,**
764 3283-3287.

765 Sun, D.-Z., 1997: El Niño: A coupled response to radiative heating? *Geophys. Res. Lett.*, **24,**
766 2031-2034.

767 ——, 2000: Global climate change and El Niño: A theoretical framework. *El Nino and*
768 *Southern Oscillation.* Cambridge University Press**,** 443-463.

769 ——, 2003: A possible effect of an increase in the warm-pool SST on the magnitude of El Niño
770 warming. *J. Clim.*, **16,** 185-205.

771 ——, 2007: The Role of El Niño—Southern Oscillation in Regulating its Background State.
772 *Nonlinear Dynamics in Geosciences*, Springer, 537-555.

773 ——, and Z. Liu, 1996: Dynamic ocean-atmosphere coupling: A thermostat for the tropics.
774 *Science*, **272,** 1148-1150.

775 ——, and T. Zhang, 2006: A regulatory effect of ENSO on the time-mean thermal stratification
776 of the equatorial upper ocean. *Geophys. Res. Lett.*, **33**.

777 ——, Y. Yu, and T. Zhang, 2009: Tropical water vapor and cloud feedbacks in climate models:
778 A further assessment using coupled simulations. *J. Clim.*, **22,** 1287-1304.

779 ——, J. Fasullo, T. Zhang, and A. Roubicek, 2003: On the radiative and dynamical feedbacks
780 over the equatorial Pacific cold tongue. *J. Clim.*, **16,** 2425-2432.

781 ——, T. Zhang, Y. Sun, and Y. Yu, 2014: Rectification of El Niño–Southern Oscillation into
782 climate anomalies of decadal and longer time scales: Results from forced ocean GCM
783 experiments. *J. Clim.*, **27,** 2545-2561.

784 ——, and Coauthors, 2006: Radiative and dynamical feedbacks over the equatorial cold
785 tongue: results from nine atmospheric GCMs. *J. Clim.*, **19,** 4059-4074.

786 Sun, Y., F. Wang, and D.-Z. Sun, 2016: Weak ENSO asymmetry due to weak nonlinear air–
787 sea interaction in CMIP5 climate models. *Adv. Atmos. Sci.*, **33,** 352-364.

788 Sun, Y., D.-Z. Sun, L. Wu, and F. Wang, 2013: Western Pacific warm pool and ENSO
789 asymmetry in CMIP3 models. *Adv. Atmos. Sci.*, **30,** 940-953.

790 Thirumalai, K., P. N. DiNezio, Y. Okumura, and C. Deser, 2017: Extreme temperatures in
791 Southeast Asia caused by El Niño and worsened by global warming. *Nat. Commun.*, **8,** 1-
792 8.

793 Thual, S., A. J. Majda, N. Chen, and S. N. Stechmann, 2016: Simple stochastic model for El
794 Niño with westerly wind bursts. *Proc. Natl. Acad. Sci. USA*, **113,** 10245-10250.

795 Timmermann, A., and F.-F. Jin, 2002: A nonlinear mechanism for decadal El Niño amplitude
796 changes. *Geophys. Res. Lett.*, **29,** 3-1-3-4.

797 Timmermann, A., F.-F. Jin, and J. Abshagen, 2003: A nonlinear theory for El Niño bursting.
798 *J. Atmos. Sci.*, **60,** 152-165.

799 Timmermann, A., J. Oberhuber, A. Bacher, M. Esch, M. Latif, and E. Roeckner, 1999:
800 Increased El Niño frequency in a climate model forced by future greenhouse warming.
801 *Nature*, **398,** 694-697.

802 Tziperman, E., S. E. Zebiak, and M. A. Cane, 1997: Mechanisms of Seasonal – ENSO
803 Interaction. *J. Atmos. Sci.*, **54,** 61-71.

804 Tziperman, E., L. Stone, M. A. Cane, and H. Jarosh, 1994: El Niño chaos: Overlapping of
805 resonances between the seasonal cycle and the Pacific ocean-atmosphere oscillator.
806 *Science*, **264,** 72-74.

807 Wang, B., and Z. Fang, 1996: Chaotic oscillations of tropical climate: A dynamic system theory
808 for ENSO. *J. Atmos. Sci.*, **53,** 2786-2802.

809 Wang, B., J. Li, and Q. He, 2017a: Variable and robust East Asian monsoon rainfall response
810 to El Niño over the past 60 years (1957–2016). *Adv. Atmos. Sci.*, **34,** 1235-1248.

811 Wang, B., and Coauthors, 2019: Historical change of El Niño properties sheds light on future
812 changes of extreme El Niño. *Proc. Natl. Acad. Sci. USA*, **116,** 22512-22517.

813 Wang, G., and Coauthors, 2017b: Continued increase of extreme El Niño frequency long after
814 1.5°C warming stabilization. *Nat. Clim. Change*, **7,** 568-572.

815 Wang, X.-Y., and Coauthors, 2021: Underestimated responses of Walker circulation to ENSO-
816 related SST anomaly in atmospheric and coupled models. *Geosci. Lett.*, **8,** 1-13.

817 Weisberg, R. H., and C. Wang, 1997: A western Pacific oscillator paradigm for the El Niño-
818 Southern Oscillation. *Geophys. Res. Lett.*, **24,** 779-782.

819 Yeh, S.-W., J.-S. Kug, B. Dewitte, M.-H. Kwon, B. P. Kirtman, and F.-F. Jin, 2009: El Niño
820 in a changing climate. *Nature*, **461,** 511-514.

821 Ying, J., and P. Huang, 2016: Cloud–radiation feedback as a leading source of uncertainty in
822 the tropical Pacific SST warming pattern in CMIP5 models. *J. Clim.*, **29,** 3867-3881.

823 Zhang, T., and D.-Z. Sun, 2014: ENSO asymmetry in CMIP5 models. *J. Clim.*, **27,** 4070-4093.

824 Zhao, Y., and D.-Z. Sun, 2022: ENSO Asymmetry in CMIP6 Models. *J. Clim.*, **35,** 5555-5572.

825 Zheng, Y., J. L. Lin, and T. Shinoda, 2012: The equatorial Pacific cold tongue simulated by
826 IPCC AR4 coupled GCMs: Upper ocean heat budget and feedback analysis. *J. Geophys.*
827 *Res.: Oceans*, **117,** C05024.